

28 anthropogenic pollution as a necessary co-factor in the occurrence of KD and sets the field to associate
29 other similar human vasculitis.

30

31 **Introduction**

32 Causes conducive to Kawasaki disease (KD) syndrome are yet unknown, despite the intensive
33 research on different fronts (genetic, immunological, environmental, epidemiological, etc., 1,2).

34 Alleged drivers include a myriad of potential factors under different hypothesis around the innate and
35 adaptive immune responses observed in KD (e.g. bacteria, fungi, viruses and toxins, 3–8) but no

36 conclusive result has unequivocally solved this long-standing puzzle. KD is an acute, self-limited
37 vasculitis that occurs in children of all ages. On the etiology, the leading paradigm is that a yet

38 unidentified agent enters through the upper respiratory tract and causes a dramatic immunologic
39 response in certain genetically predisposed children (9,10). Coronary artery aneurysms develop in

40 20–25% of cases, with this development being at times clinically silent and often misdiagnosed with
41 other more benign rash/fever syndromes caused by viruses or bacterial toxins (11). It may lead years

42 later, to sudden death or myocardial infarction (12). Seasonality of KD was first described for Japan
43 (13) and then worldwide (14). Increases in KD cases in winter in locations at both sides of the North

44 Pacific Ocean were seen to occur associated with the seasonal enhancement of low- and high-
45 tropospheric wind currents from the Asian continent (15). The ulterior identification of a fungal

46 pathogen being predominant in the aircraft profiles in Japan made on air masses over the planetary
47 boundary layer (PBL) at times of KD maxima, led to the hypothesis that KD could be caused by a

48 pathogen or environmental trigger carried out by winds blowing from the Asian continent (8,15–17).

49 The long rich record of epidemiological incidences of KD in Japan going back to the seventies enables
50 a very detailed and unprecedented statistical approximation (8,14,15,18). Now detailed analyses of

51 daily admissions of KD in epidemiological records for the entire of Japan and for 9 regions grouping
52 prefectures, clearly uncover the presence of a prominent sub-weekly cycle (SWC) along with the

53 already known strong seasonality as the dominant variability components (Fig. 1A, B). Singular
54 Spectrum Analysis (SSA) decomposition ($M=100$; see Methods and 19,20) applied to these datasets
55 separated among significant cyclical components that accounted for most of the variability in the time
56 series. Figure 1 displays for the historical daily epidemiological records of KD aggregated for entire
57 Japan, both the seasonal evolution (Fig. 1A) and a prominent SWC (Fig. 1B). An AR spectrum with
58 a backward-forward singular value decomposition algorithm was computed for KD (Fig. 1C) to
59 further determine the sources of spectral variability and assess the nature of the weekly oscillations.
60 First two Reconstructed Components (RC) recovered seasonality (RC12, 70% of the variability,
61 $p < 10^{-5}$; Fig. 1A), and a previously unnoticed SWC showed up strongly that accounted altogether for
62 a 20% of the variance. This SWC was composed by two clearly distinguishable sub-periods (Fig.
63 1C), with the fundamental one being that of 3.5 days (d) ($SWC1 > 10.6\%$; $p < 10^{-5}$), and harmonic at
64 2.33d ($SWC2 = 9.2\%$; $p < 10^{-5}$, see methods).

65 Existence of (seven days) weekly cycles in human diseases -or in clinical data- has been attributed to
66 a surrogate of the weekday-weekend dynamics in hospital admissions in poor health care locations
67 with reduced staffing levels or less experienced staff (21–23), or to lower number of admissions for
68 mild diseases or even to biases in reporting (e.g. admissions being assigned to the following Monday
69 or labor day, 24). For instance, difference in medication outcomes and even death can occur due to
70 lower quality or activity of medical care, or even delayed initiation of treatments in the case of severe
71 diseases (25,26). Lower admission rates also occur over the weekend for asthma and mild diseases
72 (27) and in prevalence surveys of nosocomial infections, due to the effects of air pollution on hospital
73 admissions and mortality (28). But most previous studies on weekday variability have focused on
74 acute admissions, such as an increased risk of myocardial infarction, ischemia, sudden death, and
75 cardiac arrests occurring on Mondays (29–33). Conversely, weekend admission in Japan was
76 associated with increased mortality in patients with severe community-acquired pneumonia (23) and
77 also with increased myocardial infarction in women (34). The association of mortality with day and

78 time of admission has been tackled by many studies, with considerable heterogeneity in the results
79 (25).

80 It is well-known that no natural weekly cycles exist, being the weekly period a cycle with a unique
81 anthropogenic fingerprint (35–37). There are natural daily circadian rhythms, seasonal or sub-
82 seasonal cycles and long term interannual changes (e.g. El Niño-Southern Oscillation, decadal
83 variability...). Human activity in industrialized countries largely follows a 7d cycle, where fossil fuel
84 combustion is expected to be reduced during weekends (38–41). This weekend effect is well known
85 from local, ground-based measurements, and may even translate into a small temperature signature,
86 associated to a reduction in transportation (42). Nitrogen oxides ($\text{NO}+\text{NO}_2=\text{NO}_x$ and reservoir
87 species) are important trace gases in the troposphere with impact on human health, atmospheric
88 chemistry and climate (e.g. due to ozone production, 43; and their influence on the OH concentration,
89 44). Some studies showed the weekly cycles of tropospheric NO_2 for different regions of the world
90 (42), with a clear minimum in the US, Europe and Japan and even with 35% lower NO_2 levels on
91 Sundays than on working days in Germany (45).

92 In the current study, we first separate KD variability and address the origins of the SWC components
93 from the long epidemiological records of KD in Japan. After carefully discarding the influence of a
94 potential weekend bias, we move towards tracing the 3.5d SWC in KD to temporally co-vary with
95 the same variability existing in atmospheric particulate matter (PM_x) and wind dynamics over Japan.
96 Atmospheric PM_x composition and movement are then tracked by means of the Asian dust and aerosol
97 LIDAR observation network (AD-Net) (46,47). LIDAR profiles are also scrutinized to search
98 whether wind intrusions from the mid-troposphere are associated to both aerosol peaks and KD peak
99 maxima seasons. We further describe the time taken by these air intrusions to affect and originate
100 recognizable KD increases. Finally, we investigate the potential relationship of KD incidence to the
101 PM_x chemical composition, specially to airborne metals.

102 To determine the base frequencies in daily KD records, we conducted a two-way Scale-Dependent
103 Correlation (TW-SDC) analysis (48–50) as it is specifically aimed at uncovering transitory
104 associations between joint variability structures in time series (see methods). We used the daily series
105 of KD in the recent interval for which we also have LIDAR atmospheric profiles (2010 in Fig. S1 and
106 January 2010-December 2016 in Fig. S2), and a synthetic time series of 3.5d (SWC1), 2.33d (SWC2)
107 and 7d (SWC3) periods (see Methods). Fig. S1 displays the TW-SDC for SWC1(a,d), SWC2 (b,e)
108 and SWC3 (c,f) at different window sizes, s ($s=6d$ in a,b,c and $s=22d$ in d,e,f) for the year 2010. The
109 prominent role of the 3.5d cycle (SWC1) stands out clearly, both in terms of correlation magnitude
110 as well as of presence throughout 2010-2016 (a vs c, d vs f and Fig. S2). In addition, a very faint
111 SWC3 (7d) essentially derived from the 3.5d cycle, correlates instead to periods with very low KD
112 incidence (Fig. S1c and f). A similar analysis with an intermediate s of 10 to maximize a potential 7d
113 cycle applied to the entire 2010-2016 interval further reinforces instead the more dominant role of
114 SWC1 in KD (Fig. S2). This way, two maxima and two minima clearly exist in a week and the SWC
115 strongly shows up in all the large epidemics (Fig. 2A, for the largest KD epidemic, in 1982; Fig. S3
116 for 1979, 1982 and 1986). SWC1 exists throughout the entire KD epidemiological record since
117 surveillance was initiated in the early 1970s in Japan (and up to the latest data available at the end of
118 2016, Fig. 2B). Concomitant capricious behavior at both minima and maxima during the largest
119 epidemic is not consistent with a systematic reporting bias on Sundays-Mondays (8).

120 To assess whether geographical coherence exists for this SWC1 period throughout Japan, a specific
121 analysis tracing the presence of the 3.5d was conducted for the main 9 large aggregations of
122 prefectures in Japan (Fig. 2B) (see Methods). As seen, contribution of this variability is roughly
123 constant throughout the entire record (seen since 1977 when separate prefecture information is
124 available).

125 The former stability in the SWC1 amplitude is true also for all groups of individual prefectures,
126 irrespective of their population, with the exception of Okinawa for which there is a marked

127 enhancement of the SWC in the last few years (Fig. 2B). Despite, as said above, no natural cycles are
128 described that have a weekly or semi-weekly periodicities, we further checked whether bias-reporting
129 could have generated those persistent periodicities. The latter was totally discarded as the SWC cycle
130 amplifies towards the present concomitant with the appearance of coherent marked seasonality in the
131 epidemiological time series (8,15). Fig. S3 shows the reconstructed SWC(top) for the three main
132 epidemics in Japan (1979, 1982 and 1986), together with the individual contribution of the different
133 RCs of the SWC, namely SWC1 (3.5d; second row), SWC2 (2.33d; third row). Daily OW SDC
134 analysis of KD per prefecture at $s=7d$ was further conducted and strong positive correlations close to
135 the diagonal counted and grouped annually for the entire of Japan (Fig. 2B, black line; see Methods).
136 Results shows a clear enhancement of the SWC1 towards the present, a rising trend and also an
137 intriguing 4-year oscillation, discussed elsewhere (8). Total yearly aggregated KD incidence for Japan
138 (red line) is there shown for comparison (Fig. 2B), with a slightly steeper upward trend towards the
139 present, as well as an absence of the formerly described 4-year period. This same 4-yr period can be
140 seen in the bottom panel of Fig. 2B, computed with monthly data instead. The increase in the number
141 of times air intrusions is associated with more KD events might be thought to be driven by changes
142 (increases) in wind intensity. Instead, close analyses show that despite the mean gradient of winter
143 (DJF) regional wind stress for the interval 1975-2015 in northeast Asia clearly points to a straight
144 connection between NE Asia and Japan (8) (Fig. S4A), there were not regional changes in the trends
145 of wind stress nor in zonal and meridional wind speed during winter occurred (Fig. S4B). Instead
146 warming indicates rises in northeast Asia of more than one degree Celsius on average from the 2000s
147 with respect to the seventies. Therefore, mechanisms must point either or both to a gradual
148 optimization in the direction of source winds -as indicated by the recent phase-locking of the seasonal
149 variability in both KD and winds(15)-, or to an increase in the aerosol load due to enhanced
150 anthropogenic activity in the source region.

151 To test for this possibility, we traced the SWC1 in KD, and its relation to anthropogenic activity (e.g.
152 pollution and aerosols). The latter was investigated by means of LIDAR measurements, available

153 from 2010 onwards. Fig. 3A displays the relation from 2010 to 2016 of KD monthly total cases in
154 Japan (black) and a surrogate variable tracing the presence of SWC1 in particles in the Tokyo air
155 column (SWC1-PM₁ for absc532, blue). Absc532 stands for 532nm attenuated backscatter coefficient
156 from LIDAR measurements averaged at both the surface (Fig. 3A, 4A) and at different height levels
157 for Tokyo, Toyama and Tsukuba (Fig. 4B). Attenuated backscattering ratio between 1064nm and
158 532nm (absc1064/absc532) has been described to be an excellent analog for sizes of aerosol particles
159 (51,52), yielding here values well below 1 (not shown) and therefore clearly denoting dominance of
160 particles of size below 1µm (Fig. S5). Amount of PM₁ aerosols clearly grows during events associated
161 to KD maxima (Fig. S5A). Fig. 3A displays a striking monthly (weekly in Fig. 4A) positive
162 coevolution between the SWC1-PM₁ cycle (blue) and KD incidence (black), with the presence of the
163 3.5d cycle shortly anticipating KD (Fig. 3B). Synchronous annual cycles show up in both variables,
164 with coincident maxima in winter and minima in summer, as expected. This large seasonal coherence
165 among wind and SWC1-PM₁ further reinforces the central role of aerosols in this disease.

166 Seasonality in these same variables for 2010-2016 was studied grouping monthly changes in the three
167 aforementioned variables for Tokyo, Toyama and Tsukuba (Fig. 4B). These three locations are unique
168 in that all have routine LIDAR instruments being operated from 2010-2016 ([http://www-](http://www-lidar.nies.go.jp/AD-Net/index.html)
169 [lidar.nies.go.jp/AD-Net/index.html](http://www-lidar.nies.go.jp/AD-Net/index.html)), as well as long-term KD epidemiological records. KD in Fig.
170 4B groups all dates with KD maxima by month (red: 90% threshold, see Methods).

171 To expand on results above, we applied an SDC correlation analysis (48,49) in Fig. 3B between the
172 same two variables during 2010-2016. A strong link between them appears that enhances towards the
173 present, and denotes a leading role for airborne particles on KD (top series). This lead is clearly
174 evident as strong positive associations (red dots) denote correlation values above +0.6 and up to +0.8
175 ($p < 0.01$) (see black box in lower panel) present at and below the main diagonal. Atmospheric PM
176 over Tokyo was studied in relation to the WC up to 6km height and the direction of their movement
177 traced (53). This way, downward direction in the air column of particles arriving at Tokyo (PM₁

178 analog: blue line, see Fig. S5 and Methods for the PM_{10} size determination) (51) is shown in Fig. 3A
179 (monthly) and Fig. 4A (weekly) for the entire 2010-2016 interval, together with wind speed (red line)
180 and KD incidence (black line). Clear covariation is evident between PM_{10} and KD maxima occurring
181 both also at times of maximum wind speed, and not with higher air column stability. These maxima
182 correspond to air intrusions and downward motion over Tokyo as indicated by the black box in the
183 monthly averaged LIDAR atmospheric profile. High(Low) seasonal concentration of aerosols exists
184 in the surface due to strong(weak) downward winds typically occurring in winter(summer) since 2010
185 (Fig. 3A, 4A). Both monthly (Fig. 3A) and weekly (Fig. 4A) evolution in the three aforementioned
186 variables further reinforce this strong co-variation. Predominance of the SWC1 at different heights
187 clearly displays a downward movement as denoted also by SDC analyses, with larger amount of
188 SWC1 variability decreasing as we move down the atmospheric profile. Despite causality cannot be
189 directly inferred, results strongly point towards a consistent link among them all and to the
190 involvement of tropospheric aerosols in the epidemiology of KD.

191 Fully coherent seasonal changes exist also in SWC1- PM_{10} both over the PBL (σ PBL, blue) and at the
192 surface (surf, green) in the three locations. Daily delay between the disease and SWC- PM_{10} at both
193 the surface (Fig. 4B, right column) and over the PBL (Fig. 4B, central column), supports their relation
194 at a daily time scale since the lagged distribution is zero-centered (see also Fig. S5B). Dominance in
195 all three locations occurs at zero lag, indicating there is no daily delay between occurrence of
196 maximum in both atmospheric particles and KD incidence.

197 **Association of metal elements in PM_{10} particles and KD**

198 To further explore the characteristics of particles potentially related to KD outbreaks, we used daily
199 monitoring of PM_{10} ($PM_{10} < 10\mu m$) and their chemical analyses for Kumamoto (southwest of the
200 Japanese archipelago) in spring 2011. Nearly 60 major and trace element concentrations (mostly
201 metals) were determined from filter samples collected over 37 consecutive days (see 54 for a full
202 description of the analytical methodology). Results demonstrated a remarkable covariation when

203 compared to similar elements measured at 33 air quality monitoring stations in urban, suburban and
204 rural areas operated by the Kumamoto Prefectural Government (see also
205 <http://taiki.pref.kumamoto.jp/kumamoto.taiki/index.htm>). Fig 5A shows the stunning covariation
206 between the total daily content of metals (Met_{tot} , red line) and KD incidence (KD_{03} , denoting sum of
207 new cases that are diagnosed the same day or up to three days later, black line) in Kumamoto.
208 Covariation of KD_{03} with most abundant individual elements is evident also throughout the 37 days
209 of the monitoring campaign, with predominance of certain metals (e.g. Zn, Pb, Mn, Ba, Cu, As, Se,
210 Bi and Tl) (Fig. S6). A linear regression fit was the best model relating metals in Fig. S6 (Se, Cu, Pb,
211 Zn, Ba, Mn, Bi, As) and KD cases recorded in days 0 to 3 (Fig. S7 and Table SI, with lowest AIC:
212 43,018; r^2 : 0,727, $p=5,08 \cdot 10^{-7}$). Percentage of variance accounted for by metals in that specific
213 atmospheric event rose up to over 50%, reaching values near 60% in the case of Zn (Fig. S7; Table
214 S1). A linear regression model denotes how an increment of around 70 ng/m^3 in the concentration of
215 total metals is associated with a new KD case (Fig. S7). Further SSA analyses applied to the total
216 amount of metals in Fig. 5A yielded clear separation of variability into four pairs of significant
217 components, namely two in Fig. 5B having a 15d periodicity that quite stably varied as the oscillations
218 reconstructed for KD_{03} . Two other paired components in Fig. 5C recover exactly the SWC in KD,
219 being the 15d cycle harmonic of the SWC. Strikingly, coarse particulate matter (denoted by PM_{10})
220 and total carbon content (C_{tot}) in Fig. 5B and 5C also display the same two main periods above, albeit
221 they peak with slight delay in the later part of the survey and with a growing (convoluting) amplitude.
222 Both C_{tot} and PM_{10} are not concurrent with neither Met_{tot} nor KD_{03} instead, whereas interestingly,
223 Fig. 5B and 5C show how the evolving amplitudes of the reconstructed SWC components are exactly
224 the same between metals (Met_{tot}) and KD_{03} (often with even a one-day lead time).

225 In the interval of roughly one month of daily sampling, different atmospheric situations were
226 described that gave rise to the varying PM_{10} chemical composition described in Fig. 5 for metals and
227 C_{tot} . A first event around 17-27 March 2011 with NW winds feeding in transient diluted waves of
228 aerosols from Asian mainland, originated temporary peaks of the fine particulate fraction ($0.5\mu\text{m}$ –

229 2.5 μ m) and yielded spikes in several metals (54) (Fig. S6). Metals are enriched in varying degrees in
230 the different size distributions and varying concentrations of Zn and Pb and to lesser degree also Mn,
231 Ba, Se and Cu are evident with coherent PM₁₀ and C_{tot} loads, denoting a mixture of dust and aerosol
232 of small sizes (*not shown*). A mixture of dust and pollution aerosols from different parts of East Asia
233 (e.g. stagnation over central China, Gobi Desert plume from the NW and agricultural debris) creates
234 a complex air quality plume. Exposure to some of the main metals found (e.g. Zn, Cu and Pb) has
235 shown high correlation with pulmonary inflammation by inhalation toxicology studies using animal
236 models (55). The long- and short-term exposure to these hazardous air pollutants, individually or
237 collectively, may cause respiratory (eye, nose, throat and sinus) irritation, allergic dermatitis and
238 adverse cardiovascular effects (56). Exposure to abundant, highly oxidative, metal-rich pollution
239 nanoparticles is a plausible route into cardiovascular pathogenesis (e.g. concentrations up to ~22
240 billion magnetic nanoparticles/g of ventricular tissue were found in hearts) (57). Inhalation of air
241 pollutants induces pulmonary oxidative stress and inflammation and presence of soluble transition
242 metals in PM_x enhances the inflammatory responses via increased oxidative stress and the release of
243 reactive oxygen species (58). Fine (PM_{2.5}) and ultrafine particles (<0.1 μ m) induce innate immune
244 response via reactive oxygen species generation by transition metals and/or polyaromatic
245 hydrocarbons (59). PM_x toxicity can be modified due to concurrent bioaerosols contribution or by
246 their ability to modulate the oxidative potential of toxic chemicals present in PM_x (60). Therefore,
247 they modulate both the innate and adaptive immune responses (61–64) in ways that can be similar to
248 those observed in KD pathogenesis, although specific research along these lines is underway.

249 **Conclusions**

250 Long-standing controversy on the ultimate causes of KD as a paradigm human vasculitis, should now
251 consider that both physical and chemical nature of aerosols play a determinant role in its onset and
252 epidemiology. Previous studies had essentially addressed variability at seasonal and longer time
253 scales while discarded any detailed analyses on the day-to-day disease and aerosol changes. The

254 discovery of a consistent sub-weekly signature in all the KD epidemiological records, at both the
255 prefecture level and for entire Japan, present continuously since the early 1970s, sheds new light on
256 the necessary concurrent factors leading to KD. This variability has long been confounded by a
257 weekend bias in reporting but our results clearly show that the fundamental cycle of 3.5d does not
258 match with a mere week-end effect. Instead, variability at this scale can only be linked to the
259 anthropogenic effect on air quality with two weekly minima and maxima. These same patterns are
260 effectively traced in air particles at all levels in the lower troposphere, being enhanced at times of air
261 intrusions (and concurrent with KD maxima). Clear weekly cycles of anthropogenic origin, such as
262 for NO₂ and PM_x have been described by satellite measurements (e.g. GOME) (38,42). However, the
263 fact that SWC components altogether account at most for around 20% of the overall KD variability,
264 denotes that factors conducive to SWC are, however, not sufficient to determine alone a KD outcome.
265 The former is in agreement with other studies where seasonal-to-interannual changes were studied as
266 the main source of KD variability (15,18). For instance, trend in KD is possibly related to other
267 processes distinct to the SWC here described, e.g. increases in cropland yield and cover (65). The
268 Asian summer monsoon is known to effectively pump Asian pollutants to the upper troposphere and
269 lower stratosphere, leading to enhanced aerosol formation that are then exported to the entire Northern
270 Hemisphere (66), and tend to subside in Japan (67,68). However, although it is clear that KD
271 enhancement is associated to external air intrusions, and temporary associations with aerosol's metals
272 can even account for over 50% of the total variability in this disease, we do not discard that a similar
273 but less pronounced inflammatory effect can equally be exerted on KD susceptible children during
274 low incidence days by local air pollution. It also remains to be investigated as other studies have
275 suggested, whether embedded in aerosols and affected by their chemistry, other factors such as
276 microbes or organic side-products, in genetically predisposed children, might also be playing a key
277 role in KD pathology and in other similar vasculitis diseases.

278

279 **References:**

280

1. S. Nagata, Causes of Kawasaki Disease—From Past to Present. *Front. Pediatr.* **7** (2019).
2. E. Marrani, J. C. Burns, R. Cimaz, How Should We Classify Kawasaki Disease? *Front. Immunol.* **9** (2018).
3. K. Matsubara, *et al.*, Development of serum IgM antibodies against superantigens of *Staphylococcus aureus* and *Streptococcus pyogenes* in Kawasaki disease. *Clinical & Experimental Immunology* **143**, 427–434 (2006).
4. M. Barton, R. Melbourne, P. Morais, C. Christie, Kawasaki syndrome associated with group A streptococcal and Epstein-Barr virus co-infections. *Annals of Tropical Paediatrics* **22**, 257–260 (2002).
5. M. N. Lee, *et al.*, *Mycoplasma pneumoniae* infection in patients with Kawasaki disease. *Korean J Pediatr* **54**, 123–127 (2011).
6. D. Y. M. Leung, *et al.*, Toxic shock syndrome toxin-secreting *Staphylococcus aureus* in Kawasaki syndrome. *The Lancet* **342**, 1385–1388 (1993).
7. T. Yoshioka, *et al.*, Relation of Streptococcal Pyrogenic Exotoxin C as a Causative Superantigen for Kawasaki Disease. *Pediatr Res* **53**, 403–410 (2003).
8. X. Rodó, *et al.*, Tropospheric winds from northeastern China carry the etiologic agent of Kawasaki disease from its source to Japan. *PNAS* **111**, 7952–7957 (2014).
9. A. H. Rowley, S. C. Baker, J. M. Orenstein, S. T. Shulman, Searching for the cause of Kawasaki disease — cytoplasmic inclusion bodies provide new insight. *Nat Rev Microbiol* **6**, 394–401 (2008).
10. Y. Onouchi, Molecular Genetics of Kawasaki Disease. *Pediatr Res* **65**, 46–54 (2009).
11. M. S. Anderson, J. K. Todd, M. P. Glodé, Delayed Diagnosis of Kawasaki Syndrome: An Analysis of the Problem. *Pediatrics* **115**, e428–e433 (2005).
12. J. C. Burns, M. P. Glodé, Kawasaki syndrome. *The Lancet* **364**, 533–544 (2004).
13. J. Burns, *et al.*, Seasonality and Temporal Clustering of Kawasaki Syndrome. *Epidemiology* **16**, 220–225 (2005).
14. J. C. Burns, *et al.*, Seasonality of Kawasaki Disease: A Global Perspective. *PLOS ONE* **8**, e74529 (2013).
15. X. Rodó, *et al.*, Association of Kawasaki disease with tropospheric wind patterns. *Scientific Reports* **1**, 152 (2011).
16. J. Frazer, Infectious disease: Blowing in the wind. *Nature News* **484**, 21 (2012).
17. T. Maki, *et al.*, Vertical distribution of airborne bacterial communities in an Asian-dust downwind area, Noto Peninsula. *Atmospheric Environment* **119**, 282–293 (2015).

18. J. Ballester, *et al.*, Kawasaki disease and ENSO-driven wind circulation. *Geophysical Research Letters* **40**, 2284–2289 (2013).
19. M. Ghil, *et al.*, Advanced Spectral Methods for Climatic Time Series. *Reviews of Geophysics* **40**, 3-1-3–41 (2002).
20. M. D. Dettinger, M. Ghil, C. M. Strong, W. Weibel, P. Yiou, Software expedites singular-spectrum analysis of noisy time series. *Eos, Transactions American Geophysical Union* **76**, 12–21 (1995).
21. F. Cavaliere, *et al.*, Intensive care after elective surgery: a survey on 30-day postoperative mortality and morbidity. *Minerva Anestesiol* **74**, 459–468 (2008).
22. M. M. Zare, K. M. F. Itani, T. L. Schiffner, W. G. Henderson, S. F. Khuri, Mortality After Nonemergent Major Surgery Performed on Friday Versus Monday Through Wednesday. *Annals of Surgery* **246**, 866 (2007).
23. H. Uematsu, S. Kunisawa, K. Yamashita, K. Fushimi, Y. Imanaka, Impact of weekend admission on in-hospital mortality in severe community-acquired pneumonia patients in Japan. *Respirology* **21**, 905–910 (2016).
24. M. J. Barnett, P. J. Kaboli, C. A. Sirio, G. E. Rosenthal, Day of the Week of Intensive Care Admission and Patient Outcomes: A Multisite Regional Evaluation. *Medical Care* **40**, 530 (2002).
25. C. M. Bell, D. A. Redelmeier, Mortality among Patients Admitted to Hospitals on Weekends as Compared with Weekdays. *New England Journal of Medicine* **345**, 663–668 (2001).
26. M. A. Mohammed, K. S. Sidhu, G. Rudge, A. J. Stevens, Weekend admission to hospital has a higher risk of death in the elective setting than in the emergency setting: a retrospective database study of national health service hospitals in England. *BMC Health Services Research* **12**, 87 (2012).
27. J. Rosselló-Urgell, *et al.*, The importance of the day of the week and duration of data collection in prevalence surveys of nosocomial infections. *Journal of Hospital Infection* **57**, 132–138 (2004).
28. K. Y. Fung, D. Krewski, Y. Chen, R. Burnett, S. Cakmak, Comparison of time series and case-crossover analyses of air pollution and hospital admission data. *Int J Epidemiol* **32**, 1064–1070 (2003).
29. Willich S N, *et al.*, Weekly variation of acute myocardial infarction. Increased Monday risk in the working population. *Circulation* **90**, 87–93 (1994).
30. Jakovljević Dimitrije, Day of the Week and Ischemic Stroke. *Stroke* **35**, 2089–2093 (2004).
31. H.-R. Arntz, *et al.*, Diurnal, weekly and seasonal variation of sudden death. Population-based analysis of 24061 consecutive cases. *Eur Heart J* **21**, 315–320 (2000).
32. R. Manfredini, *et al.*, Monday preference in onset of ischemic stroke. *The American Journal of Medicine* **111**, 401–403 (2001).

33. V. Milosevic, M. Zivkovic, S. Djuric, V. Vasic, T. Pekmezovic, Weekly variation of hospital admissions for stroke in Nis (Serbia). *Clinical Neurology and Neurosurgery* **112**, 485–489 (2010).
34. K. Kinjo, *et al.*, Variation during the week in the incidence of acute myocardial infarction: increased risk for Japanese women on Saturdays. *Heart* **89**, 398–403 (2003).
35. X. Xia, T. F. Eck, B. N. Holben, G. Phillippe, H. Chen, Analysis of the weekly cycle of aerosol optical depth using AERONET and MODIS data. *Journal of Geophysical Research: Atmospheres* **113** (2008).
36. R. S. Cerveny, R. C. Balling, Weekly cycles of air pollutants, precipitation and tropical cyclones in the coastal NW Atlantic region. *Nature* **394**, 561–563 (1998).
37. D.-Y. Gong, *et al.*, Weekly cycle of aerosol-meteorology interaction over China. *Journal of Geophysical Research: Atmospheres* **112** (2007).
38. W. S. Cleveland, T. E. Graedel, B. Kleiner, J. L. Warner, Sunday and Workday Variations in Photochemical Air Pollutants in New Jersey and New York. *Science* **186**, 1037–1038 (1974).
39. R. V. Martin, *et al.*, Global inventory of nitrogen oxide emissions constrained by space-based observations of NO₂ columns. *Journal of Geophysical Research: Atmospheres* **108** (2003).
40. M. Kanda, Progress in Urban Meteorology :A Review. *Journal of the Meteorological Society of Japan. Ser. II* **85B**, 363–383 (2007).
41. A. Sanchez-Lorenzo, *et al.*, Assessing large-scale weekly cycles in meteorological variables: a review. *Atmospheric Chemistry and Physics* **12**, 5755–5771 (2012).
42. S. Beirle, U. Platt, M. Wenig, T. Wagner, Weekly cycle of NO₂ by GOME measurements: a signature of anthropogenic sources. *Atmospheric Chemistry and Physics* **3**, 2225–2232 (2003).
43. R. Atkinson, Atmospheric chemistry of VOCs and NO_x. *Atmospheric Environment* **34**, 2063–2101 (2000).
44. D. J. Jacob, *Introduction to Atmospheric Chemistry*, T. D. Potter and B. Colman, Wiley, 2003 (Princeton University Press, 1999).
45. B. Wickert, Berechnung anthropogener Emissionen in Deutschland für Ozonsimulationen : Modellentwicklung und Sensitivitätsstudien. *Calculation of anthropogenic emissions in Germany for ozone simulation: model development and sensitivity studies* (2001) <https://doi.org/http://dx.doi.org/10.18419/opus-1544> (November 12, 2019).
46. A. Shimizu, N. Sugimoto, I. Matsui, Detailed description of data processing system for LIDAR network East Asia. *25th International Laser Radar Conference* (2010).
47. Y. Jin, K. Kai, T. Shibata, K. Zhang, H. Zhou, Validation of the Dust Layer Structure over the Taklimakan Desert, China by the CALIOP Space-Borne Lidar Using Ground-Based Lidar. *Sola* **6**, 121–124 (2010).
48. X. Rodó, Reversal of three global atmospheric fields linking changes in SST anomalies in the Pacific, Atlantic and Indian oceans at tropical latitudes and midlatitudes. *Climate Dynamics* **18**, 203–217 (2001).

49. M. A. Rodríguez Arias, X. Rodó, A primer on the study of transitory dynamics in ecological series using the scale-dependent correlation analysis. *Oecologia* **138**, 485–504 (2004).
50. X. Rodó, M.-À. Rodríguez-Arias, A new method to detect transitory signatures and local time/space variability structures in the climate system: the scale-dependent correlation analysis. *Clim Dyn* **27**, 441–458 (2006).
51. R. G. Grainger, Some Useful Formulae for Aerosol Size Distributions and Optical Properties in (2018).
52. J.-C. Raut, P. Chazette, Assessment of vertically-resolved PM10 from mobile lidar observations. *Atmospheric Chemistry and Physics Discussions* **9** (2009).
53. Q. Bourgeois, *et al.*, How much of the global aerosol optical depth is found in the boundary layer and free troposphere? *Atmospheric Chemistry and Physics* **18**, 7709–7720 (2018).
54. T. Moreno, *et al.*, Natural versus anthropogenic inhalable aerosol chemistry of transboundary East Asian atmospheric outflows into western Japan. *Science of The Total Environment* **424**, 182–192 (2012).
55. M. Park, *et al.*, Differential toxicities of fine particulate matters from various sources. *Sci Rep* **8**, 1–11 (2018).
56. N. L. Mills, *et al.*, Adverse cardiovascular effects of air pollution. *Nat Rev Cardiol* **6**, 36–44 (2009).
57. L. Calderón-Garcidueñas, *et al.*, Combustion- and friction-derived magnetic air pollution nanoparticles in human hearts. *Environmental Research* **176**, 108567 (2019).
58. T. Godish, W. T. Davis, J. S. Fu, *Air Quality*, 5 edition (CRC Press, 2014).
59. E. S. Roberts, J. H. Richards, R. Jaskot, K. L. Dreher, Oxidative Stress Mediates Air Pollution Particle-Induced Acute Lung Injury and Molecular Pathology. *Inhalation Toxicology* **15**, 1327–1346 (2003).
60. A. Samake, *et al.*, The unexpected role of bioaerosols in the Oxidative Potential of PM. *Sci Rep* **7**, 1–10 (2017).
61. R. Miyata, S. F. van Eeden, The innate and adaptive immune response induced by alveolar macrophages exposed to ambient particulate matter. *Toxicology and Applied Pharmacology* **257**, 209–226 (2011).
62. J. Hollingsworth, *et al.*, Ambient Ozone Primes Pulmonary Innate Immunity in Mice. *Journal of immunology (Baltimore, Md. : 1950)* **179**, 4367–75 (2007).
63. A. N. Mikerov, *et al.*, Ablation of SP-A has a negative impact on the susceptibility of mice to *Klebsiella pneumoniae* infection after ozone exposure: sex differences. *Respiratory Research* **9**, 77 (2008).
64. H. Zhao, W. Li, Y. Gao, J. Li, H. Wang, Exposure to particular matter increases susceptibility to respiratory *Staphylococcus aureus* infection in rats via reducing pulmonary natural killer cells. *Toxicology* **325**, 180–188 (2014).

65. X. Rodó, *et al.*, Revisiting the role of environmental and climate factors on the epidemiology of Kawasaki disease. *Annals of the New York Academy of Sciences* **1382**, 84–98 (2016).
66. P. Yu, *et al.*, Efficient transport of tropospheric aerosol into the stratosphere via the Asian summer monsoon anticyclone. *PNAS* **114**, 6972–6977 (2017).
67. N. Tsunematsu, T. Sakai, T. Nagai, Strong capping inversion over the Tokyo metropolitan area associated with airborne Asian dust. *Geophysical Research Letters* **33** (2006).
68. T. Mizuno, H. Kondo, Generation of a local front and high levels of air pollution on the Kanto plain in early winter. *Atmospheric Environment. Part A. General Topics* **26**, 137–143 (1992).

1 **Acknowledgements and Data access:** KD datasets were kindly provided by Prof. Y.
2 Nakamura at Jichi Medical Hospital by means of Japan nationwide surveys. LIDAR data
3 were kindly provided by Atsushi Shimizu and the AD-Net database at NIES, Tsukuba
4 (<http://www-lidar.nies.go.jp/AD-Net/index.html>). We would like to thank Jane Burns,
5 Teresa Moreno, Xavier Querol, Dan Cayan, Josep-Anton Morgu , Atsushi Matsuki and
6 Hiroshi Tanimoto for their helpful assistance and data sharing. This research was
7 conducted with the financial support of the European Union’s Horizon 2020 research and
8 innovation programme under Grant Agreement No.813545 at the ADAPT SFI Research
9 Centre at Trinity College Dublin. We also acknowledge the Daniel Bravo Foundation for
10 their financial support through a research grant to WINDBIOME, the HELICAL ITN EU
11 Marie Curie and the KD parents’ association Asenkawa for both their economic and
12 enthusiastic support.

13 **Author’s contributions:** X.R. took the leading role in the conception and design of this
14 study, A.N.-G. participated in the design, X.R., A.N.-G., S.B., J.C.B., T.K., A.M. and Y.
15 N. participated in the acquisition of data, A.N.-G. and X.R. analyzed the data and all
16 authors participated in the interpretation of data and discussion of results. X.R. drafted
17 the article and all authors edited and approved the manuscript.

18 **Code accession:** All codes are available on request to the corresponding author.

19 **Figure Captions**

20 **Figure 1. Long-term evolution of Kawasaki disease (KD) incidence for entire Japan**
21 **(1970-2016) and weekly cycle contribution.** A) Aggregated KD incidence for all of
22 Japan (black) and reconstructed variability at the seasonal to interannual timescales (red,
23 corresponding to RC12 of the SSA decomposition; see Methods for spectral

24 decomposition and reconstruction (19). B) Same as A) but for the weekly cycle
25 variability, decomposed into individual cycles in C). Top panel: AR Spectrum of the KD
26 time series with FB (forward-backward) singular value decomposition algorithms and
27 bottom panel: results for individual sub-weekly frequencies obtained (namely 3.5d and
28 2.33d, respectively), and exploration of different orders for stability of results.

29

30 **Figure 2. Weekly cycle in KD throughout the historical epidemiological record**
31 **(1970-2016).** A) Example of an SDC analysis applied to the daily KD epidemiological
32 dataset aggregated for the entire Japan during the 1982 epidemic (see Fig. S3 for the three
33 largest epidemics). Due to the dataset daily resolution, the SDC cannot resolve cycles
34 shorter than 4 days, albeit the resulting 7d SWC clearly shows up as alternating diagonal
35 stripes. Notice the absence of the periodicity only in short intervals. B) Presence of the
36 SWC in the long-term temporal reference evolution of KD incidence in Japan (red,
37 relative scale), for all Japan prefectures altogether (black) and for each of the nine main
38 regions in Japan (colored). Y-axis displays the sum of days with positive correlations
39 close to the diagonal per year at lag 7 obtained from a one-way SDC (OW-SDC) analysis
40 of the KD time series at $s=7d$ and $\alpha=0.05$ (Y). In the X-axis the time interval is in
41 years (X). Evolution follows the same behavior in the maxima and linear ascending trend
42 after them. This last variable is set as a reference and it has been scaled according to the
43 plot dimensions. C) Average presence of the SWC1 (3.5d) in the four abs532 LIDAR
44 atmospheric layers and evolution of the KD monthly sum of cases. Values on the Y-axis
45 are the weekly cycle mean presence magnitude along the four atmospheric layers (see
46 Methods for an explanation of methods to quantify the presence of the weekly cycle).

47

48 **Figure 3. Association of particle-inferred abundance (absc532) arrival to Tokyo and**
49 **KD cases in Japan.** A) Temporal evolution of KD in Japan (black), Tokyo atmospheric
50 PM₁ arrival with SWC1 (3.5d) dynamics (absc532, blue; SWC-PM₁) and wind speed
51 (dark red); monthly integrated. Black box denotes surface air intrusions of windborne
52 particles from high altitudes (circa 6km). These intrusions are displayed in the monthly
53 averaged LIDAR profile for absc532. B) TW-SDC analysis between the WC1 series in
54 absc532 LIDAR-inferred particle concentrations over Tokyo (top series) and KD weekly
55 total cases in Japan (left series). Analyses in B) are performed over weekly data (week 1
56 to week 313 covering the total interval of time between January 2010 and December
57 2016). Window size (s) for B) is 52 weeks, corresponding to one year. Bars there denote
58 Spearman correlation values and bottom panel shows average maximum correlations per
59 week in a time lag going from 0 (phase) up to 15 weeks (with absc532 leading KD as in
60 the black box).

61

62 **Figure 4. Coherence among LIDAR stations in seasonality, weekly association**
63 **(Tokyo) and daily synchronicity of external PM arrival dynamics (WC1) with KD**
64 **in Japan.** A) Top panel denotes the weekly association between PM₁ arrival in Tokyo
65 with SWC1-PM₁, blue) and KD in Japan (black). This vertical transport, from 4.3-6km
66 towards the surface (120-600m), is once more backed by the wind speed (red) covariation
67 (same methodology and analysis as Fig. 3A (top) in weekly scale). B) Co-evolution of
68 KD and synchrony with the 3.5d cycle (SWC1) both over the PBL and in surface air over
69 three LIDAR stations. Left) Seasonality in KD maxima (red) for the entire Japan and
70 absc532 with SWC1 over the PBL (oPBL, blue) and at the surface (surf, green). Bars are
71 normalized in respect to the total amount of maxima (KD), correlation values (absc532)

72 per month. Middle) Histograms of the lag in days between absc532 respect to KD maxima
73 oPBL, normalized by the total amount of dates from KD maxima. Right) Idem as Middle
74 but at the surface. Rows indicate Tokyo (top), Toyama (middle) and Tsukuba (bottom).

75

76 **Figure 5. Relationship between air chemistry and new cases of KD during air**
77 **intrusions at the Kumamoto prefecture (south of Japan).** A) Co-evolution of
78 Kawasaki disease increase in cases and total metal concentrations in a 37–days
79 continuous surface air monitoring campaign at Kumamoto (Kyushu, see methods). KD
80 cases are integrated over day 0 (arrival of air masses) and up to day+3 (KD₀₃) to capture
81 patients arriving from day zero to manifest the disease three days after (8). B) SSA
82 reconstructed variability at the bi-weekly time scale (see methods and 19) in the case of
83 total metals (brown), total carbon (green), PM₁₀ (red) and KD (black). C) Same than B)
84 but for the weekly reconstructed components. Note consistencies and differences among
85 phases and convoluting amplitudes of the reconstructed signatures in the different
86 variables. Embedding dimension for the SSA analysis was always varied between
87 $30 < M < 50$ to check for signal stability ($p < 0.05$). Concentration is in ng/m³ for MET_{tot}
88 and in µg/m³ for Ct and PM₁₀.

89

90 **Methods:**

91 **Datasets**

92 Epidemiological data used in this study for Japan are total daily counts of KD patients
93 admitted to hospitals for each of the 47 prefectures of Japan. To account for possible
94 effects of different population sizes in cities, incidence was also calculated for comparison
95 in the case of major Japanese cities from population censuses interpolated from 10 years

96 national demographic records and only small differences emerged with results obtained
97 for cases. KD cases were then weighed against the total pediatric population in that
98 prefecture, with data covering the interval 1977–2016 (see KD case ascertainment
99 protocol for Japan sites) (8, 15). The Japanese KD time series is derived from the biannual
100 national surveillance of all hospitals in Japan with more than 100 beds. Data corresponds
101 to 24 separate questionnaire surveys of Japanese hospitals for the period 1970–2016,
102 providing the most comprehensive record of KD cases in the world. Patient date of
103 hospitalization and prefecture of residence are recorded for each subject in the time series.
104 Time series are formed by KD patients, the date being that of hospital admission recorded
105 for all subjects. For subjects with multiple admissions, only the first hospitalization date
106 was used. To provide uniform assessment among sites, the date of admission was used as
107 a surrogate for the date of fever onset, even though for comparison with other studies, the
108 average day of KD diagnosis is normally centered on the 5th day of fever. However,
109 analyses were reproduced with calculated dates of fever onset and results did not differ
110 ($p < 0.001$, one-sided t-test). Approved written consent was obtained from all participants.
111 Human population epidemiology studies were approved by the Bioethics Committee for
112 Epidemiologic Research, Jichi Medical University.

113 NCEP/NCAR Reanalysis 1 project wind data (u-wind and v-wind components) were used
114 from 1970 to 2016 (68). Wind speed (ws) was calculated as: $ws: u = ws * \cos(\theta)$ and, $v =$
115 $ws * \sin(\theta)$. Data (m/s) was extracted from the nearest grid cell to Tokyo (LON = 138.75,
116 LAT=37.14). City population Japan was obtained from
117 <http://poblacion.population.city/japon/>.

118 LIDAR-inferred particle variable is obtained from pre-processing the AD-Net LIDAR
119 (<http://www-lidar.nies.go.jp/AD-Net/ncdf/>) NetCDF files with an R script, using the
120 package *ncdf4*. These files provide data from the following lidar parameters:

- 121 i. 532nm attenuated backscatter coefficient [1/m/sr] (absc532)
- 122 ii. 1064nm attenuated backscatter coefficient [1/m/sr] (absc1064)
- 123 iii. 532nm volume depolarization ratio (dep532)
- 124 iv. 532nm aerosol extinction coefficient [1/m] (ext532)
- 125 v. 532nm dust extinction coefficient [1/m] (extd532)
- 126 vi. 532nm spherical particle extinction coefficient [1/m] (exts532)
- 127 vii. 532nm aerosol depolarization ratio (adep532)
- 128 viii. Estimated mixing layer height [m] (hPBL)

129

130 Time and height are the two dimensions of the LIDAR parameters making them
131 spatiotemporal variables. Time resolution is 15 min, with 96 profiles per day and height
132 integrations every 30m from the surface up to 15km. These values are accumulated and
133 averaged with even higher resolution, in order to increase the signal-to-noise ratio as to
134 five range bins for height and three for time. Data is received every hour and it is
135 converted to optical parameters through a processing program. Corrected data results
136 neglect values below 120m since the accuracy cannot be computed due to limitations in
137 the geometrical overlap correction factor.

138 From the seven air particle related parameters (all except hPBL) listed previously, there
139 are three with low level data preparation: dep532, absc532 and absc1064; and four for
140 classification of scatters and estimation of optical parameters: ext532, extd532, exts532
141 and adep532 (46). These last parameters are calculated from the low-level data
142 preparation parameters. Therefore, we selected absc532 as the aerosol parameter because
143 it can detect smaller particles than absc1064, and it retrieves information about the
144 abundance and size of air particles, while dep532 its sphericity.

145 In an attempt to enhance the signal-to-noise ratio, we integrated data by atmospheric
146 layers and this way we gathered information of dynamics above and below the PBL. To
147 this end, we selected the surface level (120-600m), a height right above the PBL (oPBL,
148 1400-2500m) and two higher layers to investigate the potential external origin of aerosols.
149 The latter were layers integrating 2800-4000m and 4300-6000m heights. This distinction
150 of layers helps understanding the origin of the time series dynamics since Tokyo particles
151 are proven to follow a downwind transport (Fig. 3 and 4). Therefore, a vertical transport
152 is categorized as downwind transport if the dynamics on the higher atmospheric layers
153 anticipate that at the surface. We inferred this PM_x transport is most often external since
154 the origin is from above the PBL.

155

156 **Methods**

157 We used the SDC analysis (48-50) to study the local transitory nature of patterns
158 in every series studied as well as the local correlations existent between different
159 variables. The one-way SDC (OW-SDC) technique is an univariate method that computes
160 non-parametric Spearman rank correlations with itself using rcorr
161 (<https://www.rdocumentation.org/packages/Hmisc/versions/4.2-0/topics/rcorr>), at a
162 variety of window sizes (s). A correlation value is then obtained at a given significance
163 level ($p < 0.05$ or 0.01 , as indicated). SDC technique is sensitive to s; and therefore,
164 different s above and below the period of interest are checked to assess for consistency in
165 the results. However, despite being an optimal method for short and noisy time series, the
166 resolution it yields cannot capture all the strength of the 3.5d cycle from just daily data as
167 in the case of KD. That is because the correlation function needs at least 4 values as a
168 feasible window size, $s \geq 4$ units. This limitation has been proved by analyzing synthetic
169 time series built as $x(t) = A \cdot \cos(2 \cdot \pi \cdot F_c \cdot t)$, where F_c is the frequency, here $1/3.5$ [days⁻¹]

170 1]; where A would be the amplitude of the oscillation which is set to 1, regardless of its
171 fit with the peaks since the main interest is in phases. The OW-SDC is not able to identify
172 the 3.5d cycle, retrieve the positive off diagonal at 3.5d, when the window size was at its
173 minimum of 4d for the synthetic time series (not shown). Instead, it was able to properly
174 extract this period and the harmonic at 2.33d at larger s (namely at s=10d, such as in Fig.
175 S1 and S2; albeit with lower correlation values due to this limitation). Coherently, the 7d
176 period, a harmonic of the 3.5d (see main text and Fig. 1 and Fig. S1 and S2), was clearly
177 visible and could be used as a marker for the 3.5d cycle since s=7d. This assumption is
178 also validated by the SSA analysis which attributes the half-weekly cycle as the main
179 period, with the weekly cycle as a harmonic (Fig.1). Therefore, correlations for every
180 aggregation time series in Fig. 2B (top) were extracted from the OW-SDC correlation
181 matrix with s=7d and considering also a lag of 6-8 units below the diagonal. The three
182 off-diagonals are reduced to one by computing the mean of the positive correlation values
183 per day, resulting in a daily correlation time series. The yearly count of daily positive
184 correlations retrieves the evolution of the 3.5d cycle from its 7d harmonic.

185 An eigendecomposition analysis applied to the data covariance matrix of daily KD time
186 series in Japan and San Diego was used to partition signal contributions by frequency,
187 with the aid of adaptive nonparametric functions (69). An embedding dimension or order
188 of the decomposition of 40 was selected, as it allows a proper characterization of those
189 signals with period larger than the annual cycle, but much larger values (e.g. M=200)
190 proved totally stable in terms of both decomposition and reconstructed components (20).
191 The significance level of the spectral decomposition was computed using a bootstrap
192 method (70). The reference probability distribution function was locally computed by
193 means of 10000 white-noise time series, which were then tested against an autoregressive
194 process of order 1 having the same mean, standard deviation, and temporal one-lag

195 autocorrelation value as the interannual long-term KD time series (find further details in
196 18). An autoregressive spectrum (AR) Spectrum with three different algorithms
197 comparison with an order field ranging between values of 20 and 50 was computed on
198 the original daily KD dataset. The AR high-order model is an optimal estimator of
199 contributing frequencies as the frequencies depend only on the roots of the fitted
200 polynomial. Each spectrum is also calculated independently and intercompared. We used
201 the data singular value decomposition (SVD) algorithm for its robustness, although the
202 FB (forward-backward), Fwd (forward), and Bwd (backward) prediction variants were
203 also calculated for comparison. A 50% change in the signal subspace was also imposed
204 to test for stability in the spectral signatures and no change in resulting frequencies
205 occurred. As the data is not noise-free data, high orders were selected, well above the
206 minimum order number needed (e.g. at least double the number of expected sinusoids in
207 the spectrum). Runge-Kutta procedure was used to integrate the spectrum adaptively and
208 to achieve a proper signal-to-noise discrimination.

209

210 **LIDAR analyses and PM arrival calculations.**

211 LIDAR-inferred particle dynamics are identified by its presence magnitude, which tracks
212 a specific cycle for unit of time. SDC methodology (48-50) identifies these transient
213 dynamics in the hourly scale for absc532. For WC1, we selected the maximum correlation
214 values per hour from lags 76-92h (84 ± 8 h) computed by an OW-SDC analysis at $s=84$ h.
215 This tolerance of ± 8 h is due to the nature of data, which produces fluctuations on the 84h
216 cycle. These correlation values are then integrated in the temporal scale, providing a
217 representation of its presence for each unit of time. Therefore, presence means more hours
218 with the transient cycle favoring higher correlation values per unit of time. Presence of
219 3.5d period in absc532 is displayed in Fig. 3A (bottom) and 4A (top panel series) by

220 averaging among the 4 atmospheric layers previously described and integrating by month.
221 Both variables in Fig. 3A are smoothed by a local polynomial regression
222 (<https://www.rdocumentation.org/packages/stats/versions/3.6.1/topics/loess>) with a loess
223 method, with a second-degree polynomial and 0.1 smoothing degree parameter.
224 The PM arrival with 3.5d cycle variable from Figure 3A (top, blue), 3B and 4A (top) has
225 been computed with a two-way SDC (TW-SDC) analysis, a bivariate method. The TW-
226 SDC technique displays the transitory forcing of the atmospheric layers dynamics to the
227 surface. In this case, the driving or forcing is from 4300-6000m towards 120-600m for
228 the abs532 hourly time series. In the TW-SDC correlation matrix, the sector below the
229 main diagonal represents the delay between both time series. In this case, the window size
230 is set to 84h (3.5d) to discern the presence and interactions of WC1. The off-diagonals
231 from 0-24h are extracted and the mean value per hour is computed, since downwind
232 transport may occur within the same day. Therefore, we have now an hourly time series
233 attributed to the PM arrival with the presence of the WC1. In Fig.3A (top, blue) and 4A
234 (top), we averaged the correlations values monthly and weekly (respectively) to study its
235 relationship with the integrated wind speed and KD Japan cases. We believed that the
236 mean is a more realistic parameter than the integration, due to the nature of the data and
237 the pre-processing needed for the PM arrival with 3.5d cycle variable.

238

239 **Maximum Analysis**

240 To further explore the relationship between KD and PM_x , we developed a technique
241 called ‘maximum analysis’ for both variables during the 2010-2016 period. First, we
242 grouped KD Japan cases time series by year and computed the 90% of the values to gather
243 the maxima and additionally remove the concomitant influence of the trend. Accordingly,
244 we used the emp.hpd formula (<https://rdrr.io/cran/TeachingDemos/src/R/hpd.R>), from

245 the R package *TeachingDemos*, to find a 90% percentile of the data, an approach suitable
246 for asymmetric densities. We sorted the maxima dates by month and normalized them by
247 computing the ratio to the total number of maxima selected (Fig. 4B). This type of
248 visualization proves useful to visualize the seasonality of the KD maxima. Second, we
249 applied the methodology to track the presence of WC1 with OW-SDC, at both the surface
250 and over the PBL (1400-2500m), for the absc532 hourly time series. Afterwards, the
251 hourly timedates from the correlation values above +0.5 are gathered and sorted by
252 month. These monthly counts are normalized by the total amount of dates used to provide
253 a relative value comparable to the KD maxima (Fig. 4B left column).

254 Finally, we also computed the lag between KD maxima and the presence of the WC1 in
255 a PM_x variable above and below the PBL (Fig. 4B central and right column). These bar
256 plots display a clear distribution centered at 0, which synchronically associates the
257 different variables. Therefore, KD evolution in Japan (2010-2016) association with the
258 LIDAR-inferred particle dynamics (WC1) is coherent among LIDAR stations in
259 seasonality, weekly association (Tokyo) and daily synchronicity.

260

261

262

263

264

265

266

267

268

269

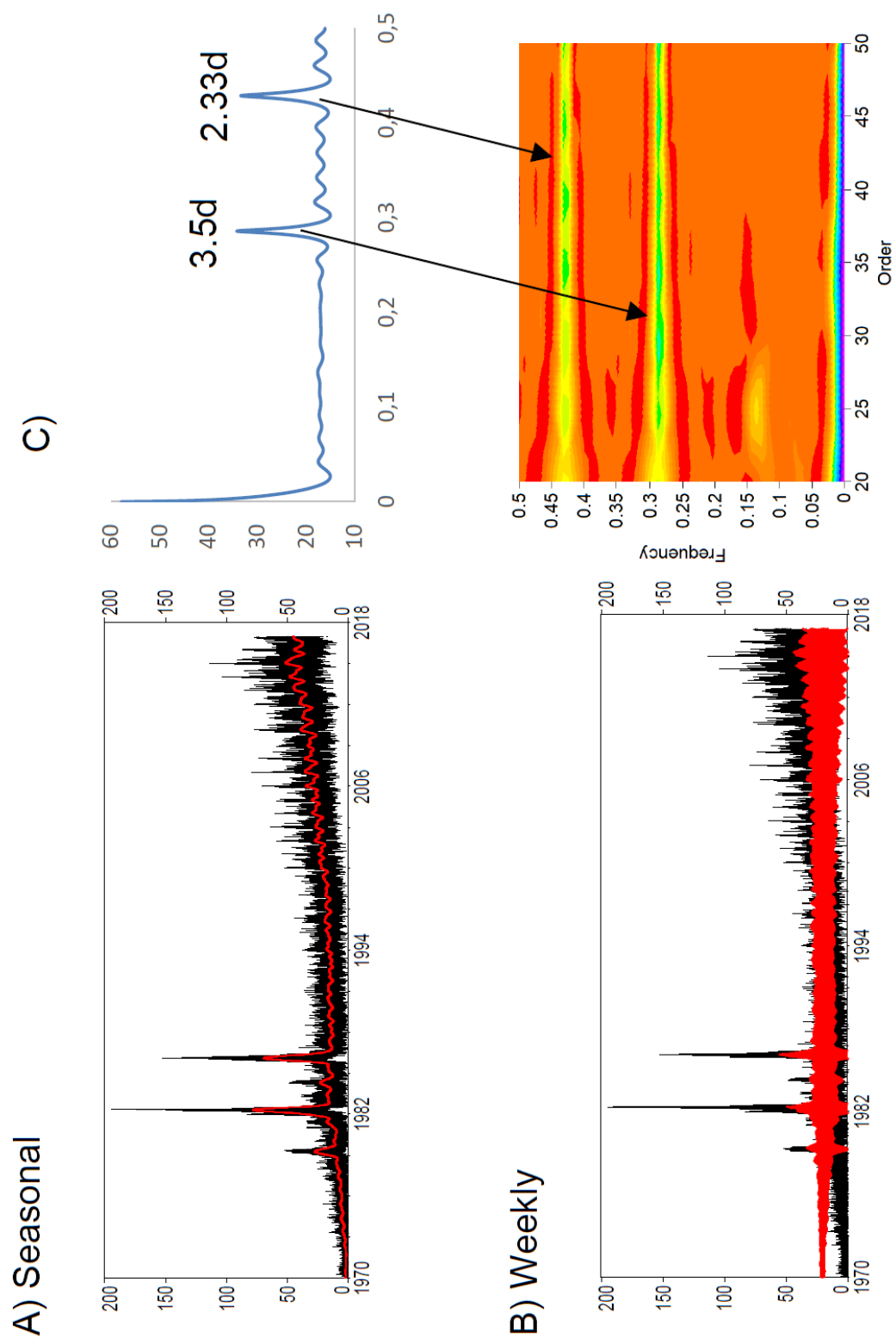


Figure 1

270
271
272
273

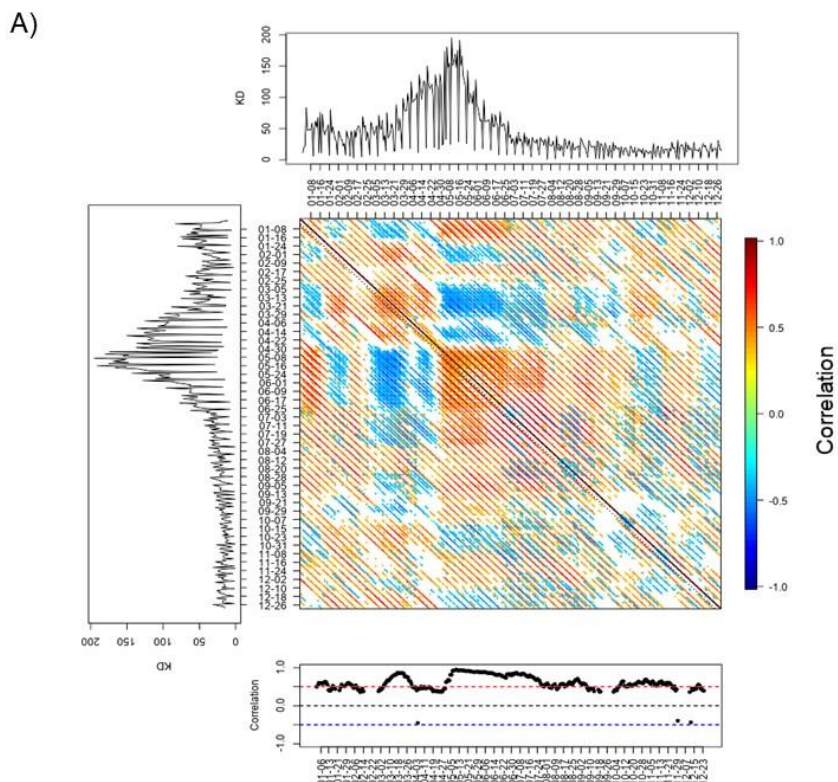


Figure 2A

274

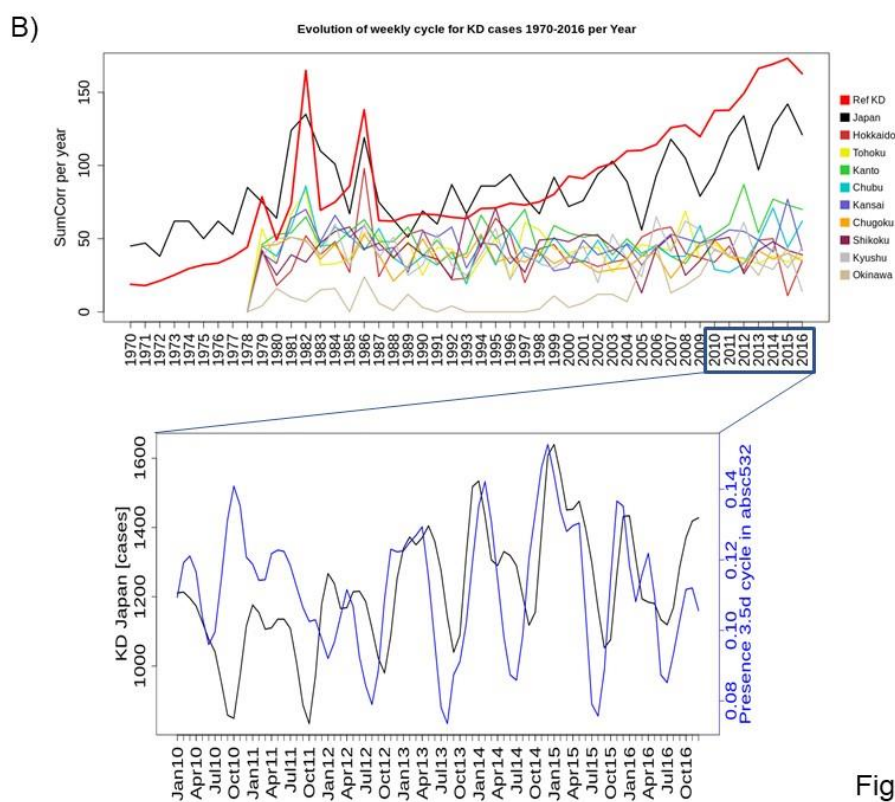


Figure 2B

275

276

277

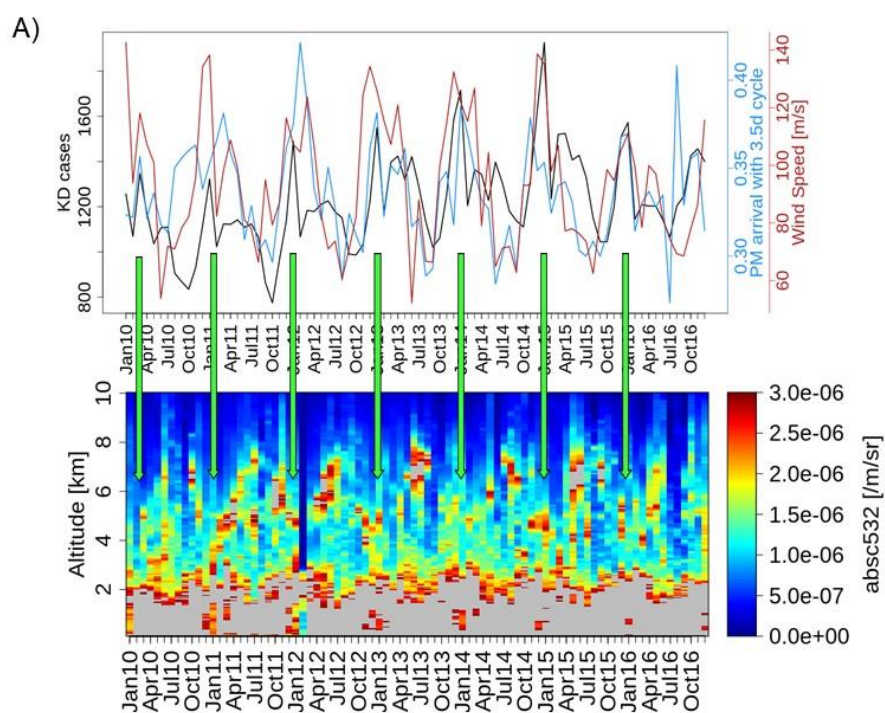


Figure 3A

278

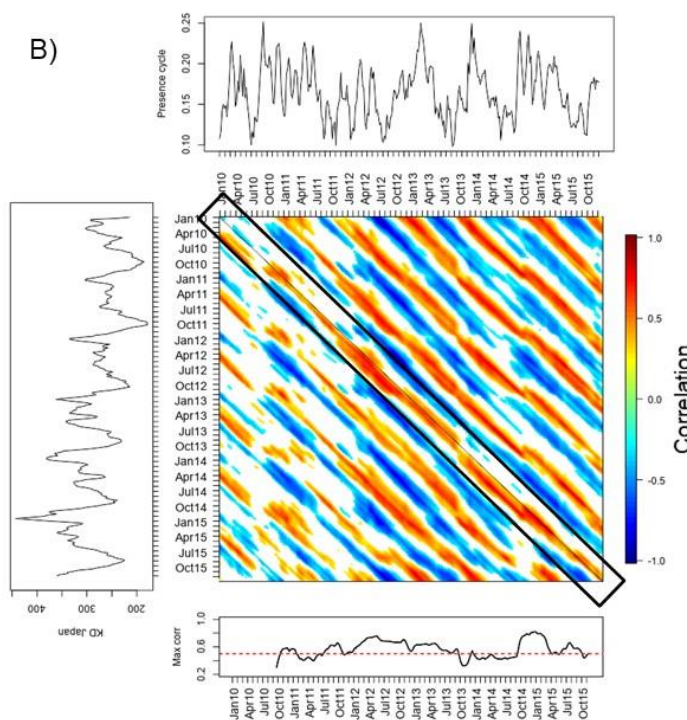


Figure 3B

279

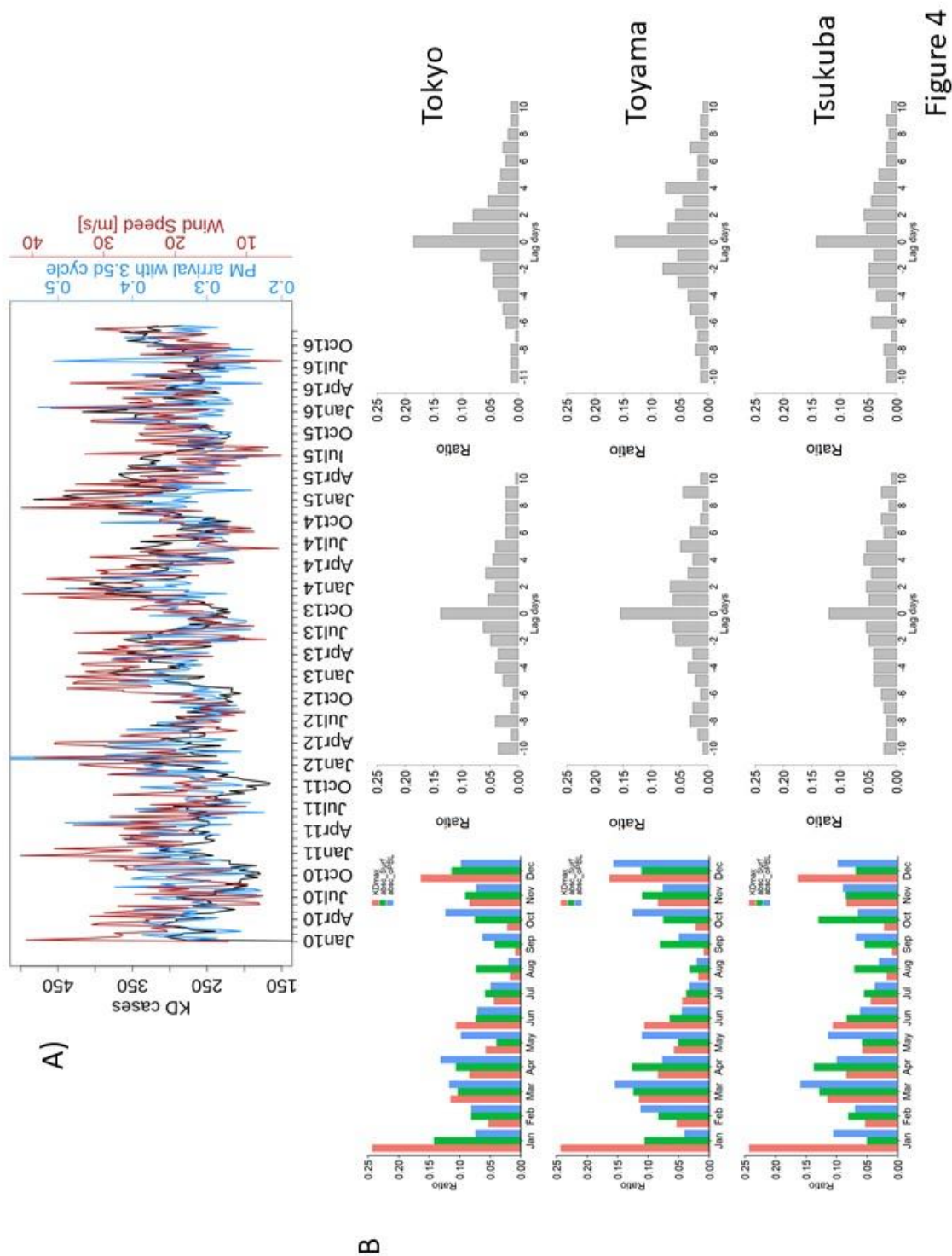


Figure 4

280
281
282
283
284

285

286

287

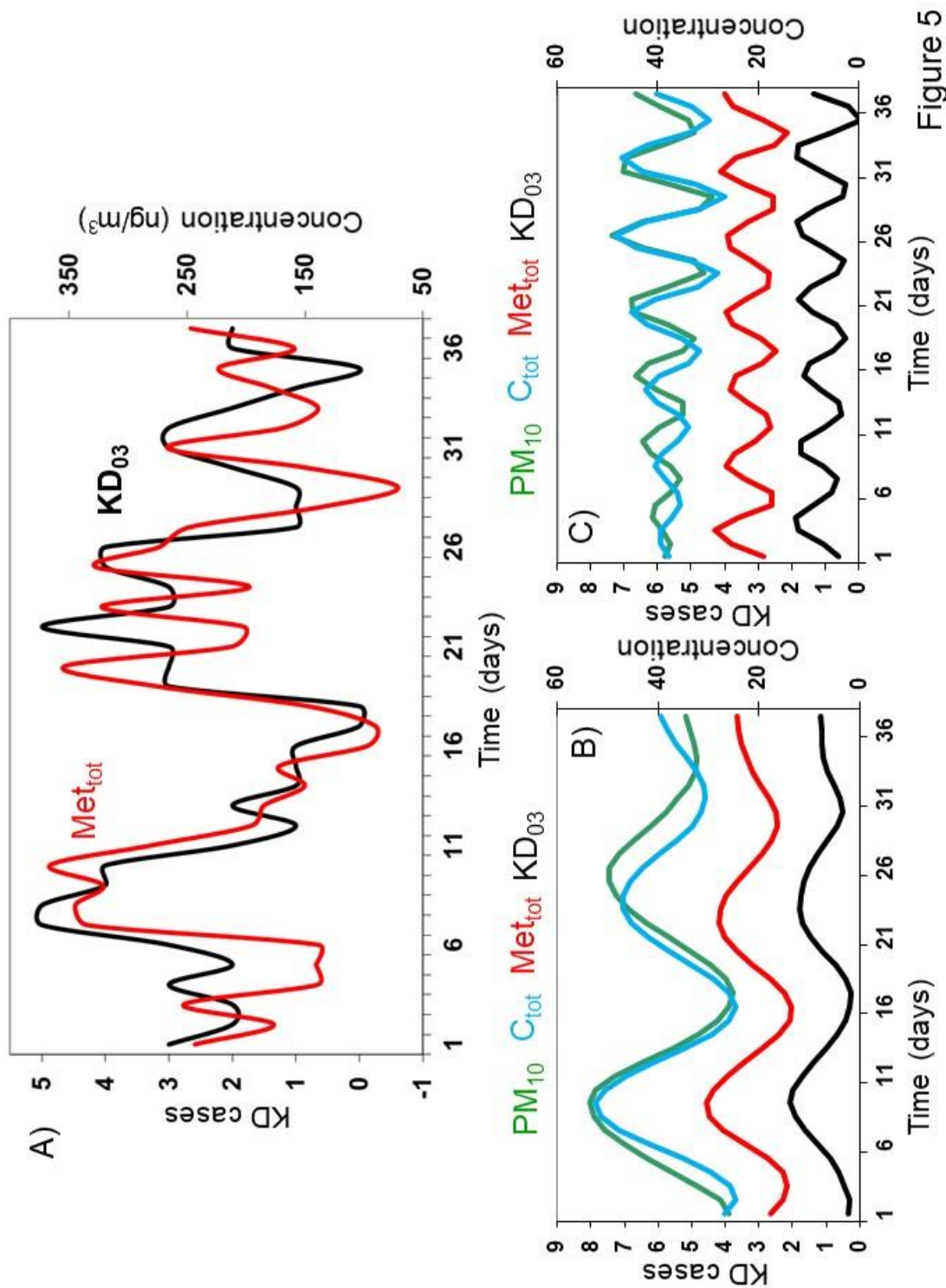


Figure 5

288

289

290 **Sub-weekly cycle uncovers the hidden link of**
291 **atmospheric pollution to Kawasaki Disease**

292

293 Rodó, X.^{1,2,†,*}, Navarro-Gallinad, A.^{2,3,†}, Kojima, T.⁴, Ballester, J.², & S. Borràs²

294

295 ¹ICREA, Barcelona, Catalonia, Spain.

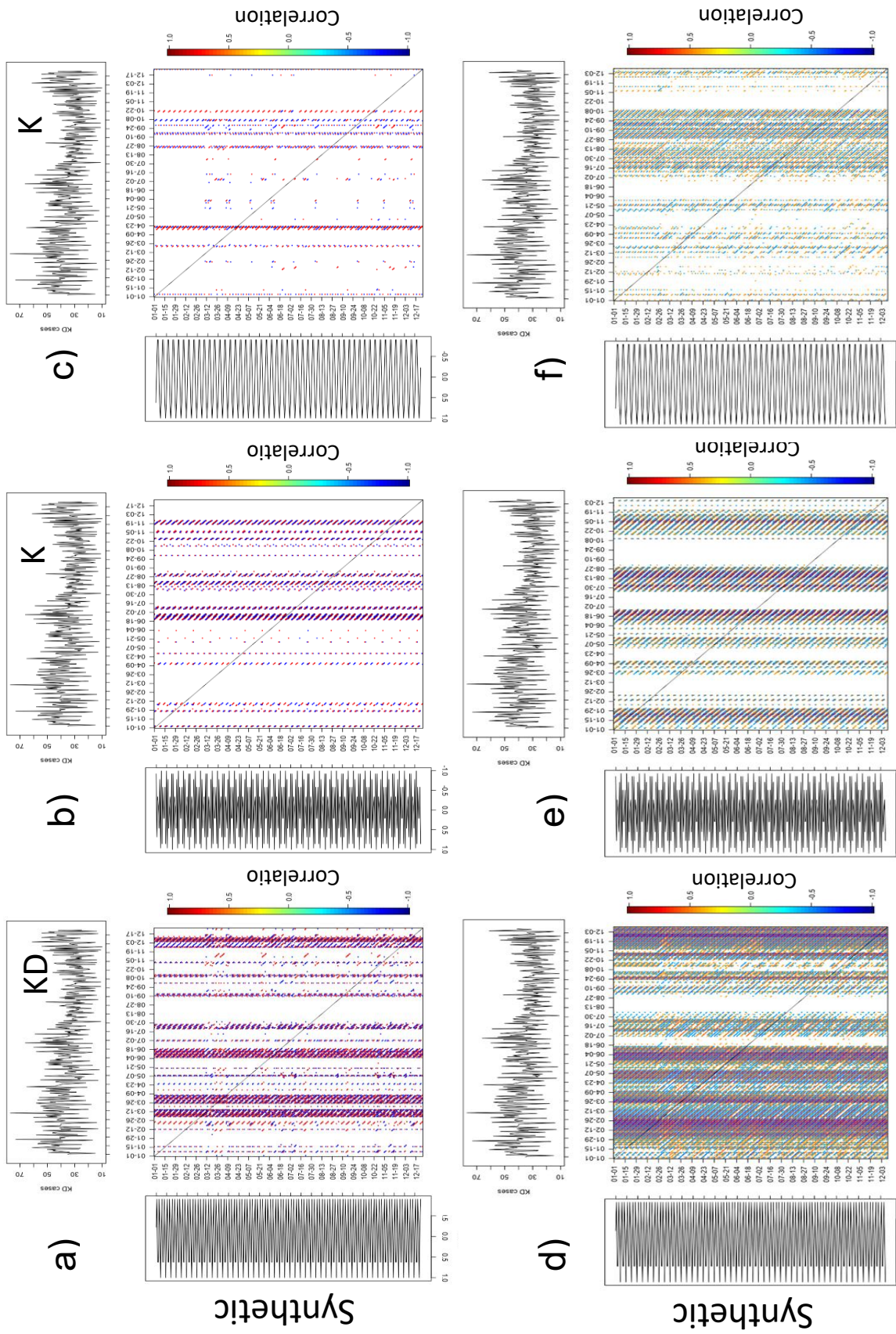
296 ²Climate and Health (CLIMA) Program, ISGlobal, Barcelona, Catalonia, Spain.

297 ³ADAPT Centre, Trinity College Dublin, Dublin, Ireland.

298 ⁴Faculty of Advanced Science and Technology, Kumamoto University, Kumamoto,
299 Japan

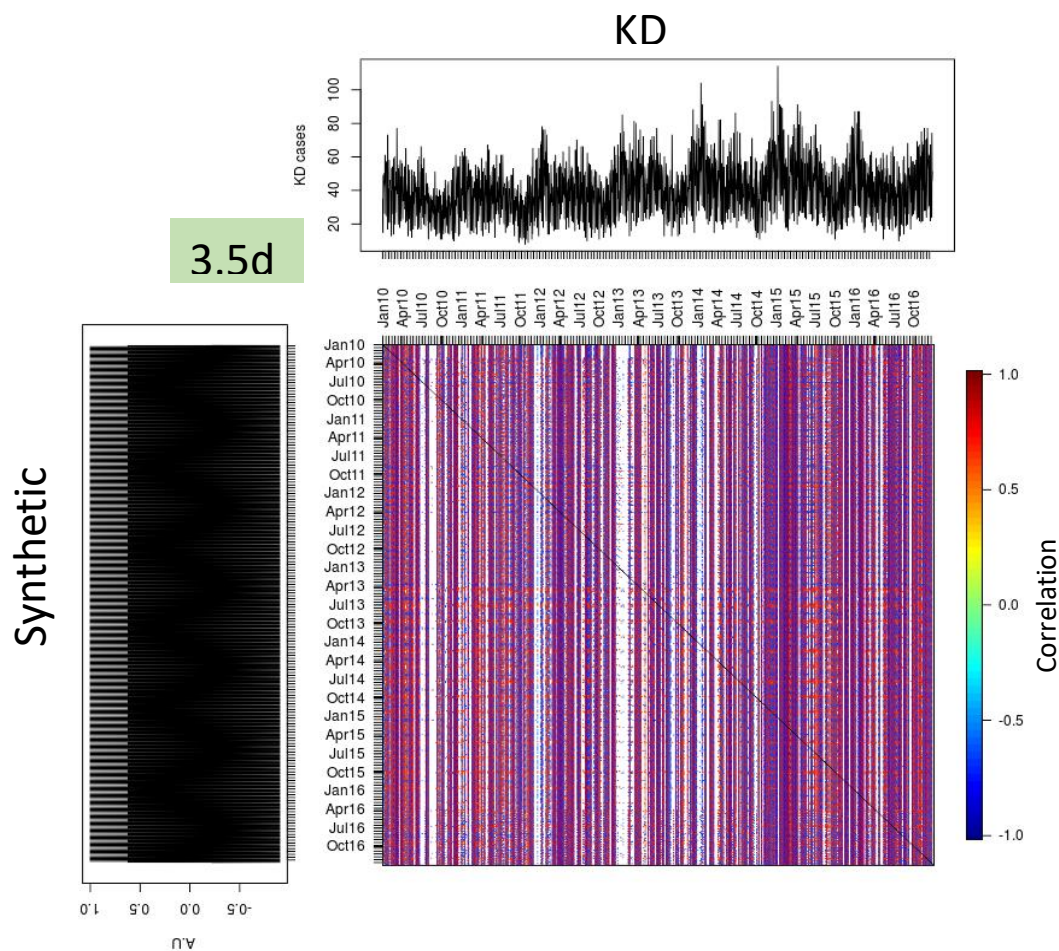
300

301 **Supplementary Information:**



302

303 **Fig. S1: Total contribution of each pair of RCs to the overall WC variability in year**
304 **2010.** TW-SDC analyses between KD in Tokyo (top series) and a synthetic series having
305 the pure WC1 (3.5d), WC2 (2.33d) and WC3 (7d) were computed for 2010 (e.g. very
306 similar patterns can be found for all years). Two different window sizes are used to test
307 for stability in the results (top, $s=6d$ and bottom, $s=22d$). WC2 is shown in middle plots
308 (b and e). Note the much larger contribution of WC1 RCs (panels a and d) than WC3
309 (panels c and f) both in their respective appearances and in the magnitude of correlations,
310 as well as the presence of the WC3 in the low KD season. WC2 is shown in middle plots
311 (b and e). Patterns displayed are significant at least at the $p<0.05$ level (see Methods
312 below for construction of the synthetic series).



313

314

315 **Fig. S2: Total contribution of WC1 to the overall WC variability in the interval 2010-**

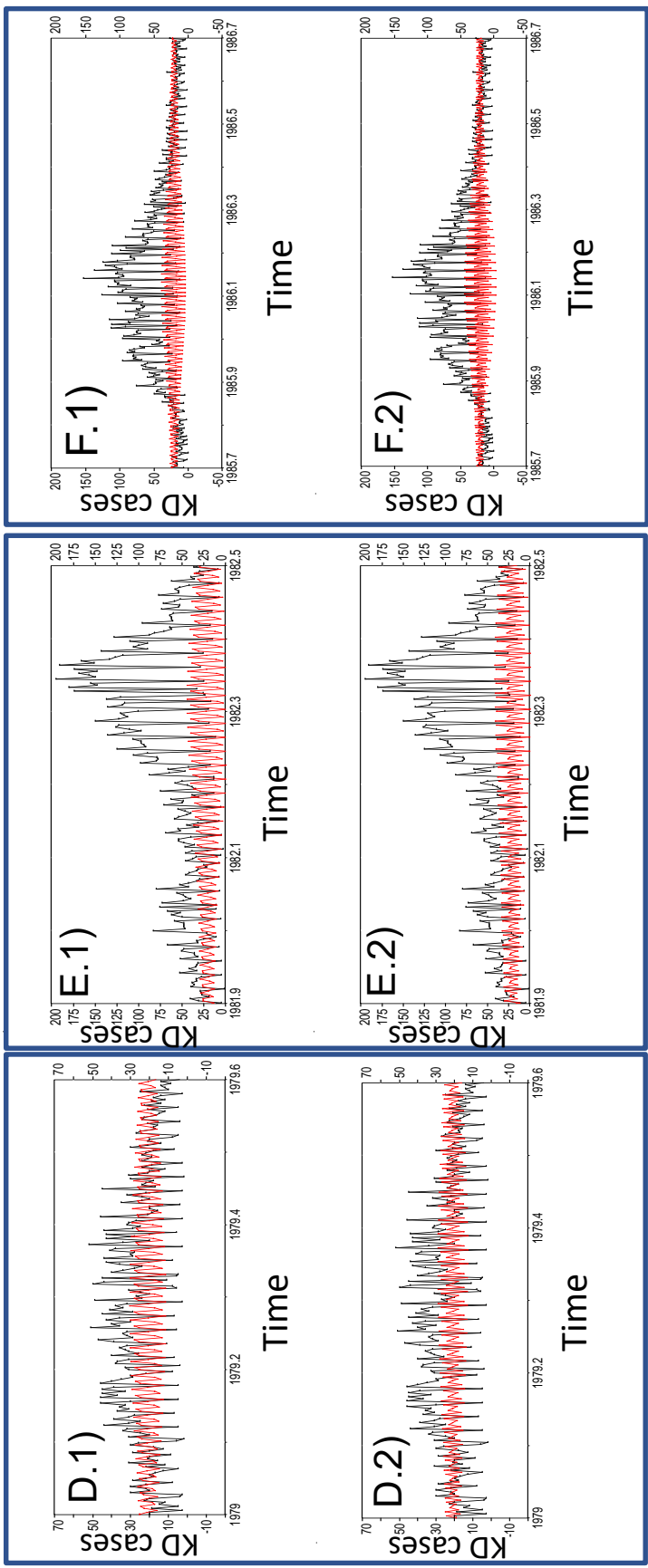
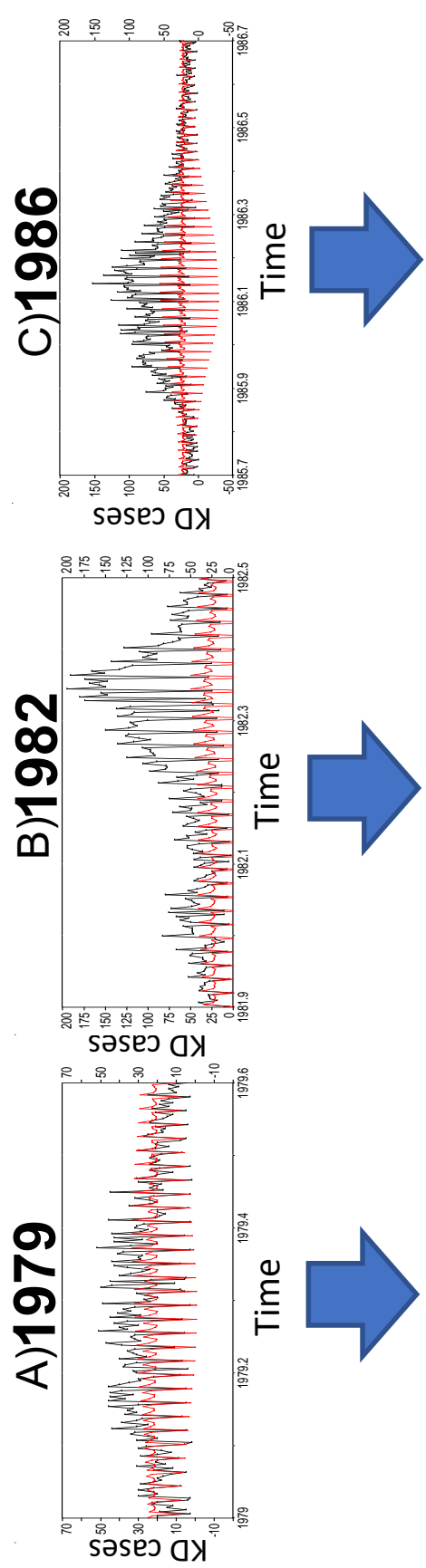
316 **2016.** Results of a TW-SDC analysis computed with the observed KD time series

317 aggregated for entire Japan and a synthetic time series with a fundamental 3.5 days'

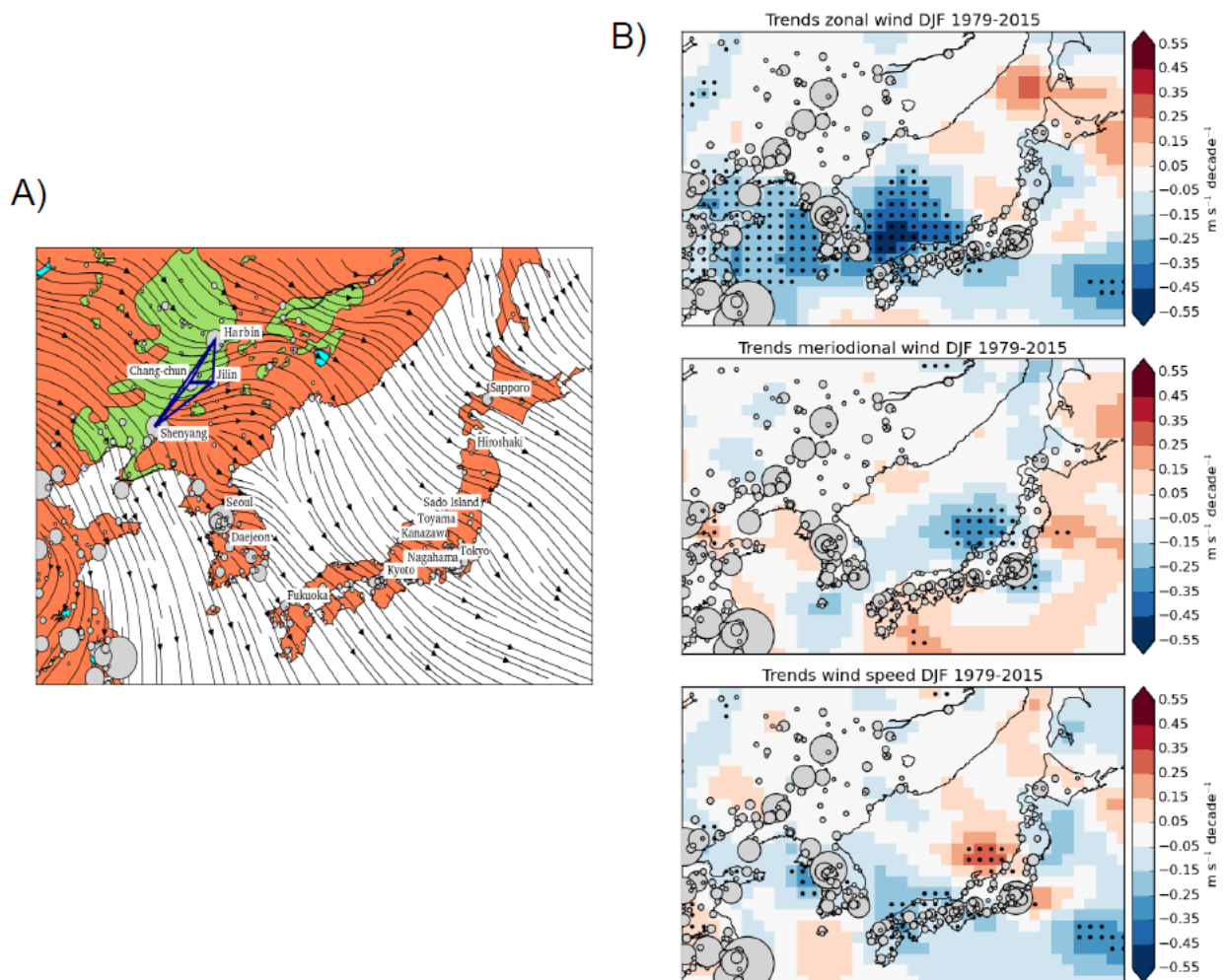
318 period. A significance threshold of 95% was imposed for correlations shown. Same

319 results also hold for Tokyo and the nine aggregated prefectures in Fig. 2B.

320

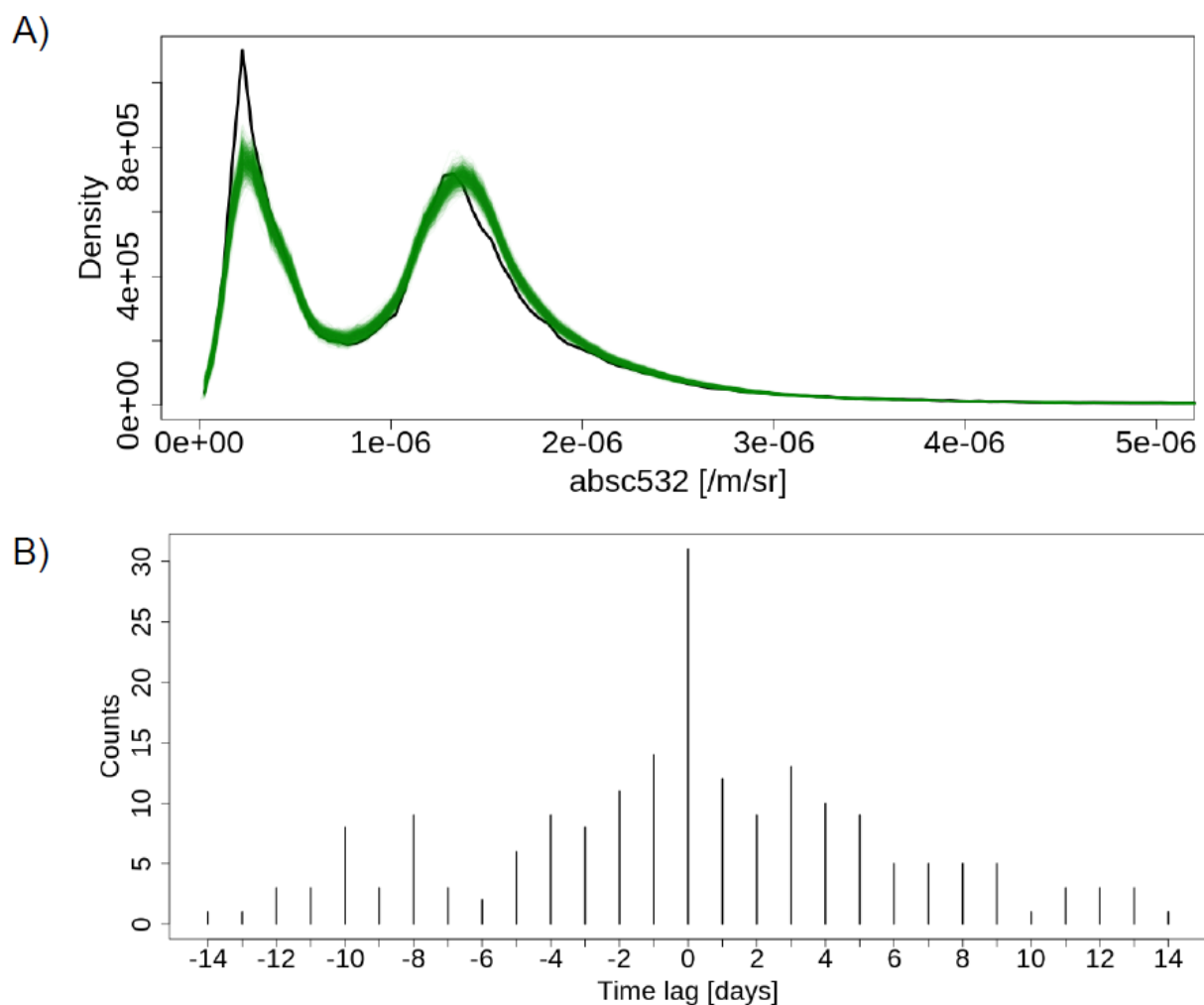


322 **Fig. S3: Reconstructed WCs in the three main KD epidemics (1979, 1982 and 1986)**
 323 **in Japan.** For each epidemic, top panels show the contribution in each epidemic of the
 324 entire WC components. Bottom panels depict the two separate RCs in each year, namely
 325 WC1 (3.5d) in D.1, E.1 and F.1; WC2 (2.33d) in D.2, E.2 and F.2. Data shown is
 326 aggregated for all Japan.
 327



328
 329 **Fig. S4:** A) Gradient of mean winter (DJF) regional wind stress for the interval 1975-
 330 2015 in northeast Asia. Cities larger than 100000 people are shown (gray bubbles). For
 331 the highlighted cities in Japan, 15 years of LIDAR atmospheric column particle
 332 composition are available. The area of intensive cereal croplands is also shown (green)
 333 together with the area main cities. B) Trends ($m*s^{-1}/decade$) in winter (DJF) zonal,

334 meridional and wind speed in the interval 1979-2015. Dotted areas denote 95%
335 significance levels.
336



337

338 **Fig. S5: Particle-size distribution in the air column for Tokyo during 2010-2016. A)**

339 Observed distribution when WC1 is present (black) vs 1000 random distributions (green)

340 in absc532 LIDAR measurements over the PBL (oPBL) in heights between 1400m and

341 2500m. B) Same as in Fig 4B (central column) but for total counts instead of ratios.

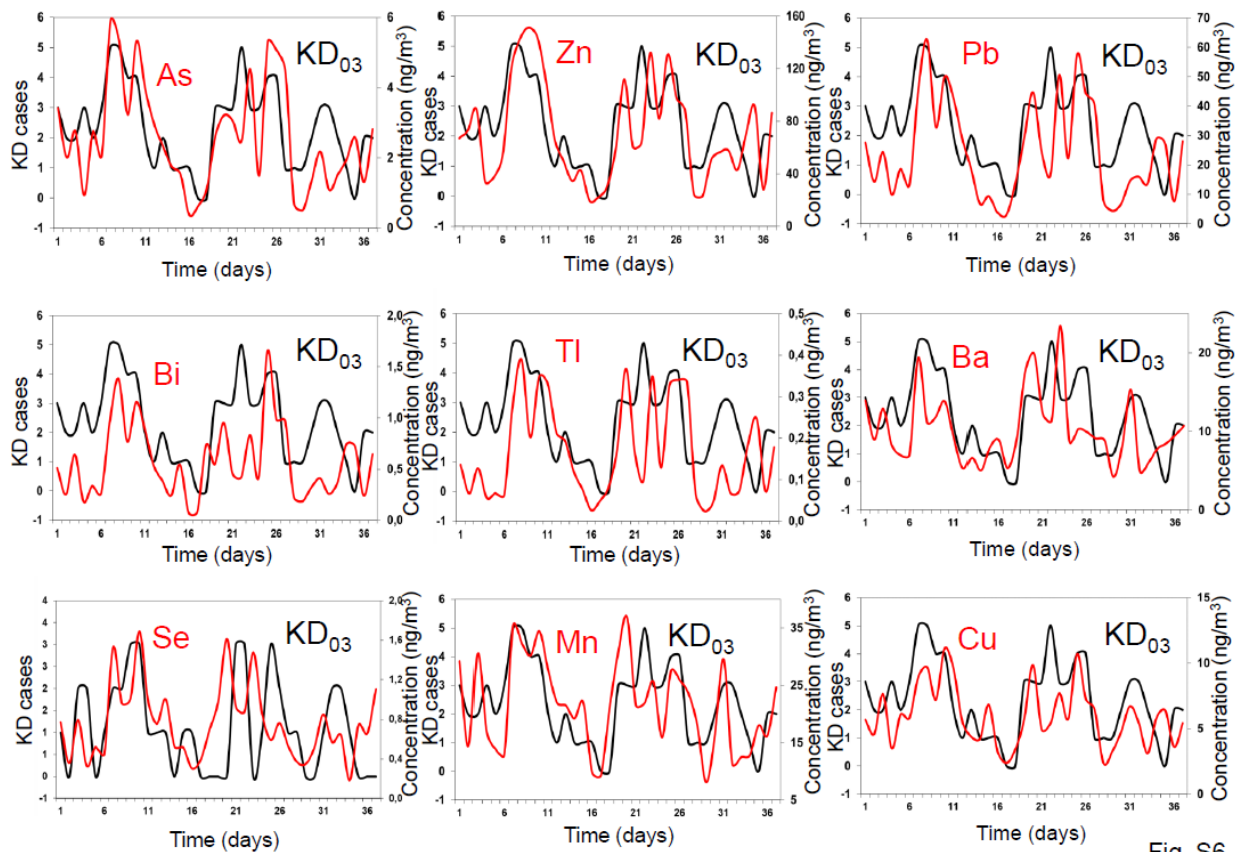


Fig. S6

342

343

344 **Fig. S6: Same as Fig. 4A but for the most abundant chemical elements (panels**

345 **displayed are for elements related to KD disease with at least $r_{xy} > +0.6$; $p < 0.05$).**

346

347

348

349

350

351

352

353

354

355

356

357 A)

B)

358

359

360

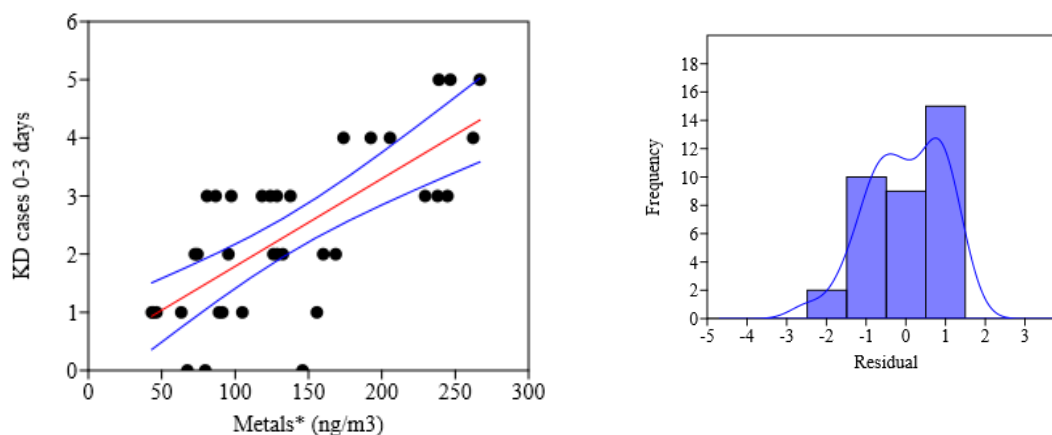
361

362

363

364

365



366 **Fig. S7:** A) Ordinary Least Squares Regression between Metals in Extended Data Fig. 6

367 (Metals* (ng/m3) state for the sum of Se, Cu, Pb, Zn, Ba, Mn, Bi and As) and KD cases

368 integrated for days 0 to 3 after air arrival (KD cases 0-3 days). B) Kernel density plot of

369 the residuals showing a bimodal distribution. 95% bootstrapped confidence intervals

370 highlighted as blue lines (N=1999). Correlation of 0,72718 ($p=5,0794 \cdot 10^{-07}$) accounts

371 locally for over 50% of total variance in KD and denotes how an increment of around 70

372 ng/m^3 in the concentration of total metals is associated with a new KD case. A linear

373 regression fit was the best model relating metals in Fig. S6 (Se, Cu, Pb, Zn, Ba, Mn, Bi,

374 As) and KD cases in days 0 to 3 (lowest AIC: 43,018; r^2 : 0,727 $p=5,08 \cdot 10^{-7}$). Fit is shown

375 below with 95% bootstrapped confidence intervals (N=1999). Similar models applied to

376 total metals yielded lower correlation values and higher AIC (45,369).

377

378

379

380

381 **Table S1.** Correlation values for all metals and KD03 in Fig. S6 (% variance also
382 displayed for highest values).

383

Variables	Correlation	p-value	lag
Zn-KD03	+0.768 (59.03%)	4.487*10 ⁻⁸	1
Pb-KD03	+0.7025	1.7887*10 ⁻⁶	1
As-KD03	+0.69373	2.7154*10 ⁻⁶	1
Tl-KD03	+0.63763	2.881*10 ⁻⁵	1
Cu-KD03	+0.62481	4.634*10 ⁻⁵	1
Mn-KD03	+0.5659	0.00026118	0
Bi-KD03	+0.55073	0.00050049	1
Se-KD03	+0.54085	0.000548	1
Ba-KD03	+0.5193	0.00098943	0
Met*-KD03	0,727 (52.85%)	5,08*10 ⁻⁷	0
Met-KD	+0,6492	1.38*10 ⁻⁵	0

384

385

386

387